Research Article | Vol. 55, No. 31 / November 1 2016 / Applied Optics 8683

applied optics

Moiré alignment algorithm for an aberration-corrected holographic grating exposure system and error analysis

XULONG ZHAO,[1,2] BAYANHESHIG,[1,*] WENHAO LI,[1] JIANG YANXIU,[1] YING SONG,[1] XIAOTIAN LI,[1] SHAN JIANG,[1] AND NA WU[1]

[1]Changchun Institute of Optics, Fine Mechanics and Physics, Chinese Academy of Sciences, Changchun, Jilin 130033, China
[2]University of Chinese Academy of Sciences, Beijing 100049, China
*Corresponding author: bayin888@sina.com

Received 15 June 2016; revised 18 September 2016; accepted 19 September 2016; posted 23 September 2016 (Doc. ID 268377); published 21 October 2016

To meet the required manufacturing accuracy of high-quality aberration-corrected holographic gratings, we propose a moiré alignment algorithm for the exposure system of holographic gratings. A model holographic grating exposure system is built with multiple degrees of freedom based on optical path function theory. The whole process algorithm is then derived, including the fourth-order orthogonal polynomial of the holographic gratings, fitted aberration coefficients, and an optimized Levenberg–Marquardt algorithm for the exposure system's recording parameters. Finally, the simulated alignment and error analysis of a 2400 gr/mm aberration-corrected holographic grating's exposure system are presented. The proposed moiré alignment algorithm for such exposure systems can effectively improve the alignment accuracy, ensuring better holographic grating aberration correction ability.

OCIS codes: (050.1950) Diffraction gratings; (050.2770) Gratings; (090.2880) Holographic interferometry; (120.4120) Moiré techniques; (120.4610) Optical fabrication.

http://dx.doi.org/10.1364/AO.55.008683

1. INTRODUCTION

Aberration correction and self-focusing are major characteristics of aberration-corrected holographic gratings. Aberration-corrected gratings, such as the concave gratings used in sophisticated spectrometry and varied line-space (VLS) gratings in synchrotron radiation experiments, have a wide range of applications in the field of spectrum measurement [1–5]. The design of aberration-corrected holographic gratings is mainly based on the optical path function theory developed by Namioka [6,7]. Laser lithographic systems use asymmetrical exposure relative to the substrate normal, as the surface of the substrate is coated with a photoresist that forms a variable groove structure, thereby providing the aberration correction capability. However, there will always be relative position alignment errors in the two recording beams of a holographic grating exposure system. This directly affects the structure of the grooves, and reduces the holographic grating aberration correction ability [8,9]. With the development of computer technology, optical design, and optical manufacturing, computer-aided alignment has become a real possibility. Egdall proposed the idea of using computer-aided alignment [10]. By researching the relevant technology, this greatly improved the accuracy of alignment in the imaging optical system compared with manual alignment. Palmer studied the holographic grating exposure system, adding two auxiliary mirrors for better aberration correction, although this increased the difficulty of adjusting the optical system [11]. Zhou *et al.* added a concave lens to the exposure system to avoid duplication between the optical elements, which produces a flat-field concave grating that uses the entire spectrum [12]. In scanning beam interference lithography, to produce the same groove density grating as a benchmark, the phase difference between the interference wavefront and the benchmark was measured, and the interference angle was adjusted in real time to change the groove density of the grating [13,14]. When the VLS grating groove density is measured by the interference field at a Lloyd's mirror system, moiré fringes are formed between the VLS grating and interference field. This enables the relative VLS grating groove density to be obtained [15]. The continuous enhancement of spectrometer specifications means that the traditional manufacturing problems of holographic gratings, such as relying on the experience of personnel, alignment blindness, lengthy manufacturing periods, and insufficient alignment accuracy, should be solved quickly. Therefore, there is a need for an improved holographic grating alignment method.

Based on the principles of computer-aided alignment in optical imaging systems, this paper proposes a moiré alignment algorithm for an aberration-corrected holographic grating's exposure system. The algorithm establishes a multidegree of freedom physical model of the exposure system, and obtains a fourth-order aberration coefficient expression for the holographic grating. In this model, the benchmark grating has a constant groove density. Using the orthogonal basis (given by Gram–Schmidt orthogonalization) of the aberration coefficient expression [16,17], moiré phase data [18–20] are applied to obtain a series of aberration coefficients. Lower-order aberration coefficients commonly feature linear recording parameters; therefore, Levenberg–Marquarat is applied to fit the recording the parameters of holographic grating. A Levenberg–Marquardt algorithm is used to determine the recording parameters of holographic grating [21], including the recording length and angle. Finally, some simulations of the benchmark grating's size, wavefront phase error, groove density, and exposure system F-number are used to analyze the primary influences on the alignment results. Through theoretical simulations, we find that the moiré alignment algorithm is a feasible measure for ensuring the alignment accuracy of the exposure system and correcting aberrations in the holographic grating. Thus, this paper explores the fabrication of high-quality aberration-corrected holographic gratings, and provides a theoretical basis for improving their fabrication precision.

2. PRINCIPLE

A. Multidegree of Freedom Physical Model of the Exposure System

Figure 1 shows a multidegree of freedom physical model of the exposure system. The system uses a Cartesian coordinate system O-xyz, where the origin O is at the benchmark grating center, the x axis is normal to the grating surface, and Oxy is the dispersion plane. Coherent point sources C and D are placed at arbitrary positions in the space. CO, DO are two recording beams of lengths r_C, r_D that form angles of γ, δ between the x-axis positive direction and angles of θ, ϕ between

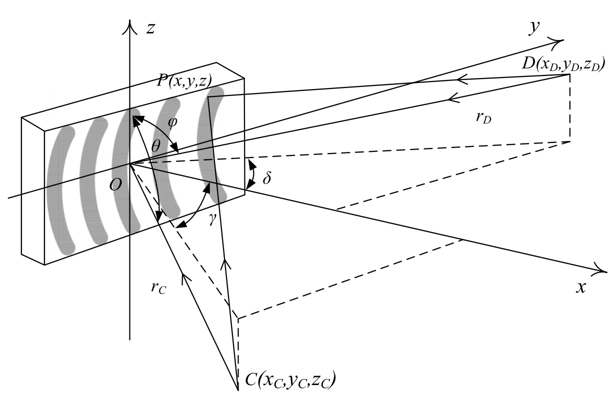

Fig. 1. Schematic diagram of a multidegree of freedom physical model of the exposure system.

the y-axis positive direction. The arbitrary point P is on the benchmark grating surface. It is known that, when the ratio of the groove density of the interference fringes and the benchmark grating is an integer, the grating surface will form some curved moiré fringes.

Based on the optical path theory of holographic gratings, the wave aberration of two coherent sources can be represented for an arbitrary point P on the grating surface as [6]

$$n\lambda_0 = (\overline{CP} - \overline{DP}) - (\overline{CO} - \overline{DO}), \tag{1}$$

where n is the groove number, which ranges from P to O, and λ_0 is the recorded wavelength in the air:

$$\begin{cases} \overline{CP} = \sqrt{(x_C - x)^2 + (y_C - y)^2 + (z_C - z)^2} \\ \overline{DP} = \sqrt{(x_D - x)^2 + (y_D - y)^2 + (z_D - z)^2} \\ \overline{CO} = r_C \\ \overline{DO} = r_D \end{cases}. \tag{2}$$

Using a Taylor expansion to give the lower-order aberration terms, the aberration function can be written as

$$\begin{aligned} E(y,z) = n\lambda_0 = {} & n_{10}y + n_{01}z + \frac{1}{2}n_{20}y^2 + n_{11}yz + \frac{1}{2}n_{02}z^2 \ldots \\ & + \frac{1}{2}n_{30}y^3 + \frac{1}{2}n_{21}y^2z + \frac{1}{2}n_{12}yz^2 + \frac{1}{2}n_{03}z^3 + \frac{1}{8}n_{40}z^4 \ldots \\ & + \frac{1}{2}n_{31}y^3z + \frac{1}{8}n_{22}y^2z^2 + \frac{1}{8}n_{13}yz^3 + \frac{1}{8}n_{04}z^4 + \ldots, \end{aligned} \tag{3}$$

with

$$\begin{cases} n_{10} = \sin\delta\,\sin\varphi - \sin\gamma\,\sin\theta \\ n_{01} = \cos\varphi - \cos\theta \\ n_{20} = \frac{\cos^2\gamma\sin^2\theta}{r_C} + \frac{\cos^2\theta}{r_C} - \frac{\cos^2\delta\sin^2\varphi}{r_D} - \frac{\cos^2\varphi}{r_D} \\ n_{11} = \frac{\cos\varphi\,\sin\delta\,\sin\varphi}{r_D} - \frac{\cos\theta\,\sin\gamma\,\sin\theta}{r_C} \\ n_{02} = \frac{\sin^2\theta}{r_C} - \frac{\sin^2\varphi}{r_D} \\ n_{30} = \frac{\sin\gamma\,\sin\theta - \sin^3\gamma\sin^3\theta}{r_C^2} - \frac{\sin\delta\,\sin\varphi - \sin^3\delta\sin^3\varphi}{r_D^2} \\ n_{21} = \frac{\cos\theta - 3\sin^2\gamma\,\cos\theta\sin^2\theta}{r_C^2} \\ \quad - \frac{\cos\varphi - 3\sin^2\delta\,\cos\varphi\sin^2\varphi}{r_D^2} \\ n_{12} = \frac{\sin\gamma\,\sin\theta(1-3\cos^2\theta)}{r_C^2} - \frac{\sin\delta\,\sin\varphi(1-3\cos^2\varphi)}{r_D^2} \\ n_{03} = \frac{\cos\theta\sin^2\theta}{r_C^2} - \frac{\cos\varphi\sin^2\varphi}{r_D^2} \\ \ldots \\ n_{04} = \frac{1}{r_D^3}(5\cos^4\varphi - 6\cos^2\varphi + 1) \\ \quad + \frac{1}{r_C^3}(5\cos^4\theta - 6\cos^2\theta + 1) \end{cases}. \tag{4}$$

In theory, the number of holographic grating aberration coefficient expressions is infinite, so it is clearly unrealistic to find them all. Thus, to meet the requirements of the discrete data fitting, we choose fourth-order aberration expressions, as this is sufficient to reduce the computational complexity while ensuring the accuracy of the fitting algorithm. Compared with the previous holographic grating aberration expression [22], Eq. (4) includes the vertical angle errors θ, φ of a coherent source, thus increasing the complexity of the aberration expression and reflecting more realistic alignment errors in the exposure system.

B. Principle of Moiré Alignment

Figure 2 is a schematic diagram of the aberration-corrected holographic grating's exposure system. M1–M4 are planar mirrors, and the beam from the He-Cd laser passes through a beam splitter (BS) to give two beams. One beam passes directly through filter F1, and the other beam is directed to the piezoelectric oscillating mirror P, which reflects the beam to filter F2. Both beams are approximately expanded into spherical waves. In the interference field, the benchmark grating's surface G forms a series of light and dark moiré fringes. A phase-locking structure is formed by the photodiode Q and piezoelectric oscillating mirror P. A CCD camera is used to capture discrete phase data of the moiré fringes.

In Section 2.A, we found that every aberration expression is a function of the exposure system of the recording parameters, interferometric phase, and recording parameters of the exposure system mapped to each other. Therefore, to obtain the recording parameters of the exposure system, we must first obtain the specific expression for the interferometric phase, that is, the holographic grating aberration coefficient. Assume that the benchmark grating's phase is $\Phi_0(y,z)$ and that the phase shift interferometry (PSI) algorithm for the moiré fringes' phase is $\Phi_M(y,z)$. Based on the principles of moiré patterns,

$$\Phi_M(y,z) = \frac{2\pi}{\lambda_0} E(y,z) - \Phi_0(y,z). \tag{5}$$

We can form the matrix of discretized phase data on the interference field, which meets the holographic grating aberration expression (3). However, when using the least mean squares algorithm to fit the holographic grating aberration coefficient n_{ij}, we must use Gram–Schmidt orthogonalization to make the aberration coefficients independent of each other in a limited aperture. Eq. (6) gives the orthogonal basis for a rectangular aperture:

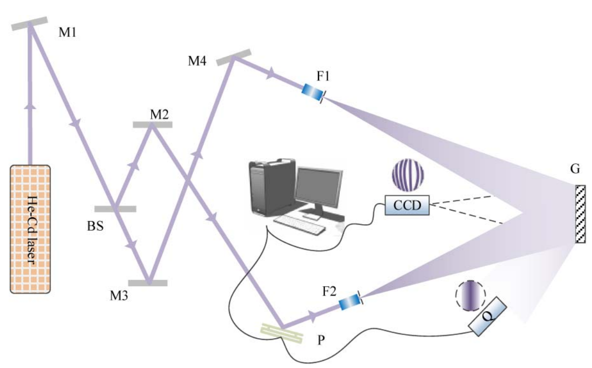

Fig. 2. Schematic diagram of the aberration-corrected holographic grating's exposure system.

$$\begin{cases} p_1 = 1 \\ p_2 = y - 1.4424e^{-16} \\ p_3 = 0.5y^2 + 1.5139e^{-16}y - 26.0625 \\ p_4 = 3.3229e^{-16}y^2 + 1.6425e^{-17}y + 0.5z^2 - 26.0625 \\ p_5 = 0.5y^3 - 1.9070e^{-16}y^2 - 46.9125y + 1.5069e^{-14} \\ p_6 = 0.5yz - 1.9488e^{-16}y + 1.3794e^{-19}y^2 + \\ +7.2391e^{-20}y^3 - 7.1899e^{-18} \\ \ldots \\ p_{15} = 1.8249e^{-14}y^4 + 2.7014e^{-19}y^3z + 3.9820e^{-16}y^3 \\ +3.2010e^{-14}y^2z^2 + 2.5149e^{-18}y^2z + 5.9047e^{-12}y^2 \\ +7.6091e^{-16}yz^2 + 4.8445e^{-17}yz + 0.125z^4 \\ -9.0831e^{-18}z^3 - 24.1232z^2 \end{cases} . \tag{6}$$

This formula represents a multidimensional space unit vector group, which is a linear representation of the holographic grating aberration expression, and does not vary with the number of aberration expressions. Thus, it satisfies Eq. (7):

$$E = [\,n_{00} \quad n_{01} \quad \ldots \quad n_{ij}\,] \begin{bmatrix} f_{00} \\ f_{01} \\ \vdots \\ f_{ij} \end{bmatrix}$$
$$= [\,n_{00} \quad n_{01} \quad \ldots \quad n_{ij}\,] \begin{bmatrix} 1 & 0 & \ldots & 0 \\ a_{21} & 1 & & 0 \\ \vdots & & \ddots & \vdots \\ a_{l1} & a_{l2} & \ldots & 1 \end{bmatrix} \begin{bmatrix} p_1 \\ p_2 \\ \vdots \\ p_L \end{bmatrix}, \tag{7}$$

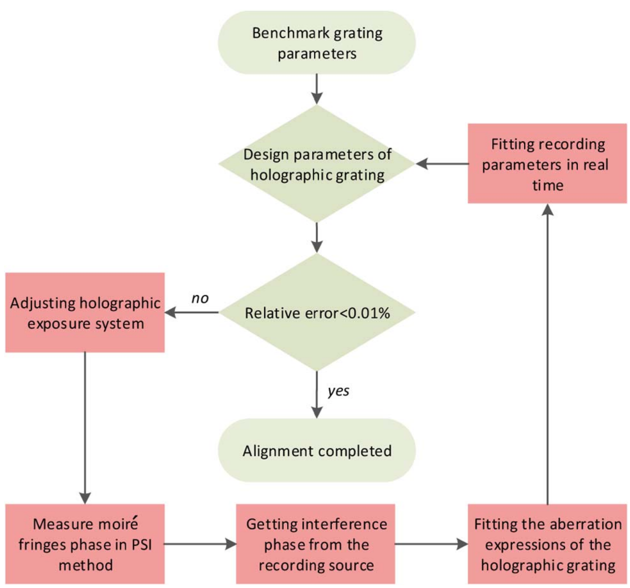

Fig. 3. Simulative process of the moiré alignment algorithm.

where f_{ij} is the holographic grating aberration polynomial and a_{ij} is the coefficient matrix of the orthogonal basis p_l. Let the difference between the realistic wavefront E_m and the estimated be as small as possible, i.e.,

$$0 = \frac{\partial}{\partial c_l}\left(\frac{1}{M}\sum_{m=1}^{M}(E_m - \hat{E}_m)^2\right) = \frac{\partial}{\partial c_l}\left(\frac{1}{M}\sum_{m=1}^{M}\left(E_m - \sum_{l=1}^{L} c_l p_{lm}\right)^2\right) \Rightarrow \sum_{k=1}^{L} c_k \sum_{m=1}^{M} p_{km}p_{lm} = \sum_{m=1}^{M} E_m p_{lm}, \tag{8}$$

where m represents element numbers in the interferometric phase matrix, $m = 1, 2, 3, \ldots M$. From the interferometric phase's orthogonal coefficient, cl is given by Eq. (7). To determine the aberration coefficient of the holographic grating at this time,

$$\begin{bmatrix} n_{00} \\ n_{01} \\ \cdots \\ n_{ij} \end{bmatrix} = [c_1 \quad c_2 \quad \ldots \quad c_l] \begin{bmatrix} 1 & 0 & 0 & 0 \\ a_{21} & 1 & 0 & 0 \\ \cdots & \cdots & \cdots & \cdots \\ a_{l1} & a_{l2} & \ldots & 1 \end{bmatrix}. \tag{9}$$

The final step is the damped least squares fitting of the recording parameters of the exposure system and comparison with the design parameter values, for which the method provides guidance for adjusting the exposure system. Figure 3 shows the simulative process of the moiré alignment algorithm.

3. SIMULATION AND ANALYSIS

To verify the feasibility of the algorithm, we examined the alignment errors of the Rowland grating, which has a groove density of 2400 gr/mm. Table 1 presents certain design parameters of the 2400 gr/mm Rowland grating.

The actual exposure system is shown in Fig. 2. Adjusting the position of filters F1, F2 relative to the benchmark allows us to measure the alignment accuracy of the exposure system. Every filter includes rotation, pitch, translation, and other five-dimensional motions. The filter moves back and forth along the beam propagation direction to regulate the recording length r_C and r_D, although this has no impact on the recording angle. When the filter moves in the vertical beam propagation direction, the recording angle and length both have an impact.

Table 1. Partial Design Parameters of 2400 gr/mm Rowland Grating

Center Groove Density d(gr/mm)	Grating Area $W \times L$ (mm × mm)	Blank Radius R (mm)	Recording Length r_C (mm)	Recording Length r_D (mm)
2400	30 × 30	750	636.0361	636.0361
Recording Angle γ(°)	Recording Angle δ(°)	Recording Angle θ(°)	Recording Angle Φ(°)	Order M
−32	32	90	90	+1

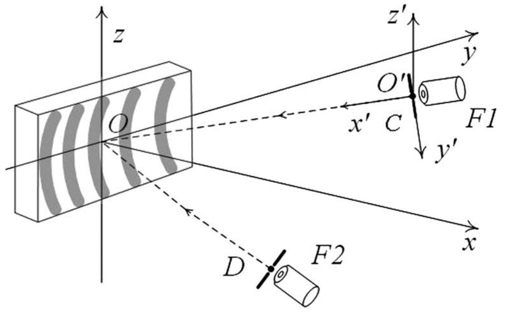

Fig. 4. Filter adjustment model.

Therefore, we have to simplify the adjustment process and decouple the magnitude of the adjustments. According to Fig. 4, the filter adjustment model defines a Cartesian coordinate system $O' - x'y'z'$, whose origin O is at the pinhole aperture in the filter. Equation (10) gives the translation values Δx_C, Δy_C, Δz_C of the recording source C under O-xyz coordinates; Eq. (11) gives the translation values $\Delta x'_C$, $\Delta y'_C$, $\Delta z'_z$ of the recording source C under $O' - x'y'z'$ coordinates. Similarly, we can obtain the corresponding values for the recording source D.

In Eqs. (10) and (11), variables with a prime denote recorded parameters obtained by the alignment algorithm, and the other variables are the holographic grating design parameters. Equations (10) and (11) can be used to obtain the adjustment direction and values directly:

$$\begin{cases} \Delta x_C = r'_C \sin\theta' \cos\gamma' - r_C \sin\theta \cos\gamma \\ \Delta y_C = r'_C \sin\theta' \sin\gamma' - r_C \sin\theta \sin\gamma \\ \Delta z_C = -r'_C \cos\theta' + r_C \cos\theta \end{cases}, \tag{10}$$

$$\begin{bmatrix} \Delta x'_C \\ \Delta y'_C \\ \Delta z'_C \end{bmatrix} = \begin{bmatrix} -\sin\theta' \cos\gamma' & -\sin\theta' \sin\gamma' & -\cos\theta' \\ \sin\gamma' & -\cos\gamma' & 0 \\ -\cos\theta' \cos\gamma' & -\cos\theta' \sin\gamma' & \sin\theta' \end{bmatrix} \times \begin{bmatrix} \Delta x_C \\ \Delta y_C \\ \Delta z_C \end{bmatrix}. \tag{11}$$

Figure 5 shows moiré fringe pictures of the error before and after the alignment process.

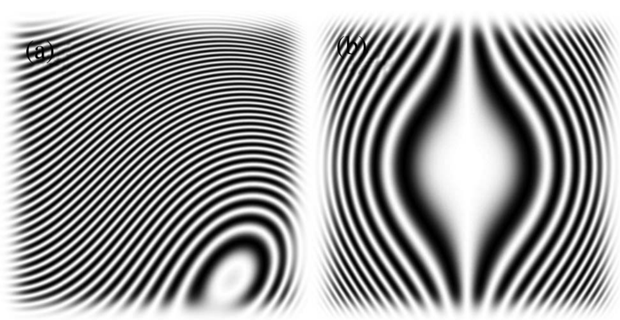

Fig. 5. Moiré fringe pictures showing the error (a) before alignment and the pattern (b) after alignment.

Table 2. Changes in Recording Parameter Values of the Exposure System Over the Whole Alignment Process

	r_C(mm)	r_C(mm)	γ(°)	δ(°)	θ(°)	φ(°)
Change in	647.5357	636.0357	−32.0200	32.0100	89.9714	89.9427
Recording	↓	↓	↓	↓	↓	↓
Parameters	636.0361	636.0361	32	32	90	90

Table 3. Corresponding Filter Adjustment Values

	$\Delta x'_C$ (mm)	$\Delta y'_C$ (mm)	$\Delta z'_C$ (mm)	$\Delta x'_D$ (mm)	$\Delta y'_D$ (mm)	$\Delta z'_D$ (mm)
Regulating Variables	−11.4993	0.2220	−0.3295	0.0013	−0.1110	−0.6360

Table 2 presents the change in the recording parameter values of the exposure system over the whole alignment process. Table 3 gives the corresponding filter adjustment values. The moiré alignment algorithm simulation results show that the algorithm can completely align the aberration-corrected holographic grating's exposure system, thus improving the alignment accuracy.

4. EXPERIMENT

To verify the feasibility of the algorithm, we performed an experimental test on grating fabricating. Figure 6 shows the experiment's instruments without the relevant computers. In the experiment, the splitter grating is driven by the piezoelectric oscillating. There are two functions splitting the laser beam and achieving a 5-step PSI algorithm. The experimental principle is described in Section 2.B. Figure 7 show moiré fringe wrap-phase pictures of the error by the 5-step PSI algorithm and unwrap-phase. We find the interference phase difference of two sources is so dozens of wavelengths, even hundreds of wavelengths, that the benchmark's wavefront error will be ignored. In other words, the moiré alignment algorithm has a large amount of tolerance.

By obtaining the unwrap-phase data, the moiré alignment we proposed calculated various recording parameters in Table 4. The following repeats the experiments five times, to verify the repeated accuracy of moiré alignment algorithm. The results show the variance of the recording length r_C and r_D is a larger value than the recording angle, because the recording length obtained is absolute position measurement, which matches the grating size and the moiré stripes position. So, it needs high accuracy measurement. In general, the repeatability and validity of the moiré algorithm is obviously verified by the experiments, but there is still further room for improvement on the accuracy of measuring the interference phase.

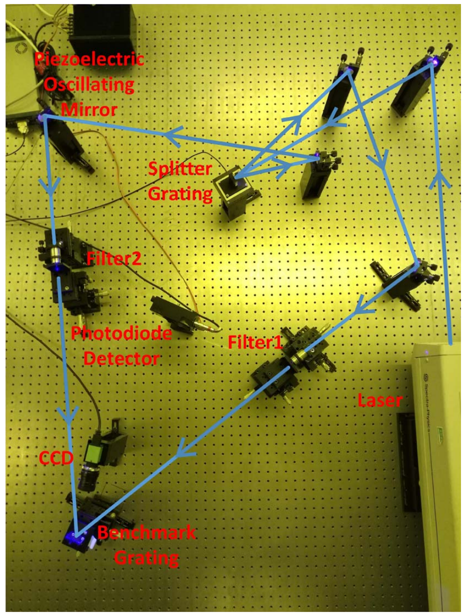

Fig. 6. Experiment's instruments without the relevant computers.

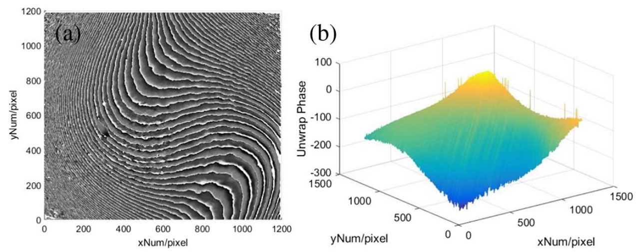

Fig. 7. Moiré fringe wrap-phase pictures (a) of the error by 5-step PSI algorithm and (b) unwrap-phase.

5. ERROR ANALYSIS

The moiré alignment algorithm gives the real-time recording parameters of the exposure system, including some fitting algorithms and measurement systems. In these algorithms, the PSI algorithm dealing with moiré fringes is widely used.

Table 4. Recording Parameters Based on the Unwrap-phase Data

Recording Parameters	r_C(mm)	r_C(mm)	γ(°)	δ(°)	θ(°)	φ(°)
1	636.9503	636.9611	−32.2651	31.7401	89.8465	89.8558
2	636.8305	636.7209	−32.3140	31.7685	89.8473	89.8579
3	636.7039	636.6947	−32.3053	31.7436	89.8467	89.8585
4	636.9500	636.7785	−32.3163	31.7502	89.8488	89.8533
5	636.6555	636.7463	−32.3244	31.7338	89.8463	89.8559
Variance	0.0186	0.0111	5.442e-4	1.764e-4	1.021e-6	4.201e-6

According to PSI theory, this algorithm does not introduce any additional error; it uses the same damped least squares algorithm, and, particularly when close to the extreme point of the linear fitting, can accurately find the corresponding extreme point. Therefore, the measurement error is mainly derived from the system itself and the order of the aberration expression. According to Eqs. (3) and (5), the change in the recording parameter ξ is related to the system's phase error ΔE. Thus, the relative error is

$$\Delta\xi = \frac{\Delta E}{A}, \tag{12}$$

$$\text{Relative Error} = \frac{\Delta\xi}{\xi}, \tag{13}$$

where $\Delta\xi$ is the increment of an arbitrary recording parameter and A is the sensitivity of the recording parameters, which is the value of the partial derivative to every variable in Eq. (3). As the recording parameters increase or decrease, the A value is changing.

From Eq. (4), it is apparent that the influence of the recording parameters on the aberration expressions of the holographic grating is symmetrical. Recording parameters γ, θ, and r_C constitute a whole, whereas δ, φ, and r_D retain the same magnitude, although they may be negated. Therefore, an error analysis of the recording parameters γ, θ, and r_C (or δ, φ, and r_D) can be employed to explain this problem. The error analysis is based on the exposure system, making a groove density of 2400 gr/mm in a Rowland grating. The grating size is 50 mm, the recording length is 636.0361 mm, and the recording angle is 32°. The following is an error analysis of the condition of the system phase error.

Figure 6 shows the influence of the benchmark grating size, the system's wavefront error, the groove density of the benchmark, and the F-number of the exposure system for each recording parameter. The following conclusions can be stated: (1) In Fig. 8(a), when the moiré phase has $1/8\lambda$ wavefront error, the alignment error of the exposure system decreases as the benchmark grating size increases. When the size of the benchmark grating is 20 mm, the relative errors in the recording length and angle are less than 0.0416% and 0.0012%, respectively. If the relative alignment error is less than 0.01%, the size of the benchmark grating should be greater than 40 mm. (2) Figure 8(b) shows that the F-number of the exposure system significantly affects the recording length. As the F-number increases, the available interferometric phase data decrease and the recording length error rises, although the relative errors remain less than 0.01%. (3) Figure 8(c) indicates that an increase in the benchmark grating's wavefront error causes the alignment error of the exposure system to grow. If the relative alignment error is less than 0.01%, the wavefront of the benchmark grating should be less than $1/5\lambda$. (4) Figure 8(d) shows that the phase error of the exposure system mainly impacts the recording angle γ of the different grating grooves. As the grating groove density increases, the relative error in the recording angle is reduced, as confirmed by the grating equation. Because the relative error of all recording parameters is less than 0.01%, this algorithm is

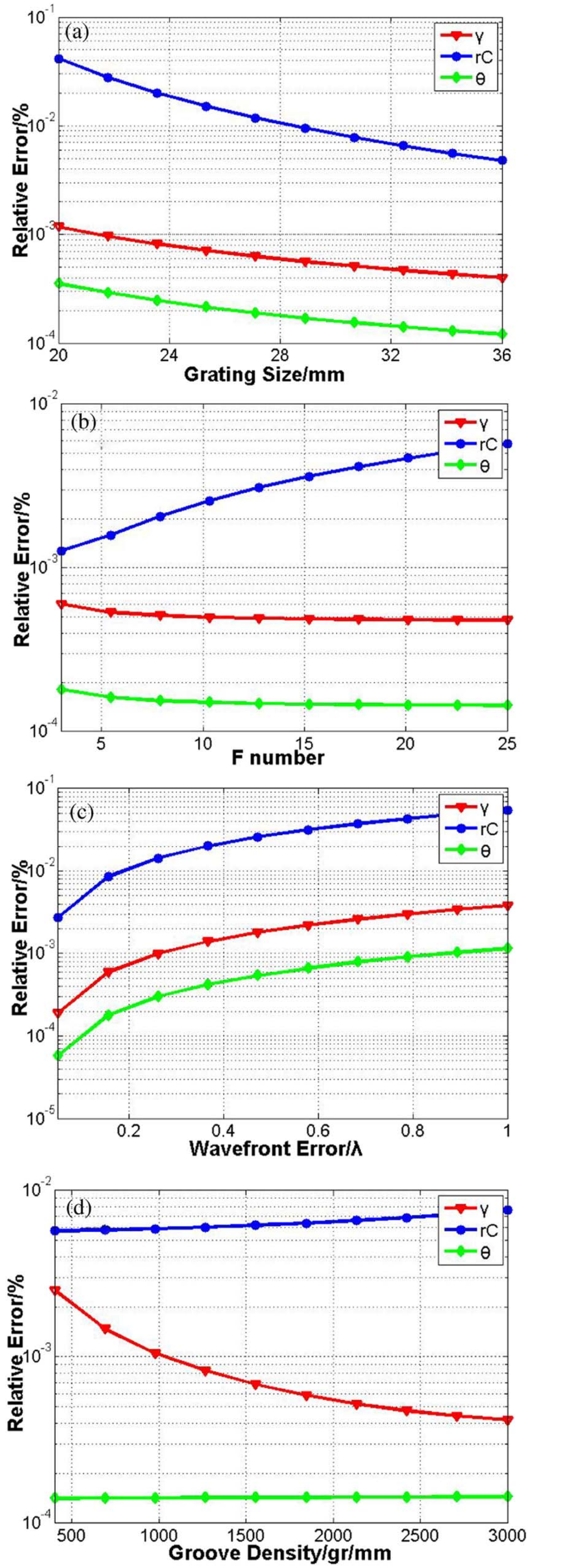

Fig. 8. Error source analysis: (a) influence of benchmark grating size on recording parameters; (b) influence of system wavefront error on recording parameters; (c) influence of groove density of benchmark grating on recording parameters; (d) influence of F-number of exposure system on recording parameters.

applicable to different groove density gratings. (5) The relative error is most strongly affected by the recording length, followed in turn by the meridional angle and the sagittal pitch.

6. CONCLUSION

In this paper, we have proposed a moiré alignment algorithm that ensures the accuracy of exposure system alignment and enhances the holographic grating's aberration-correction ability. The proposed system overcomes certain problems in the process of fabricated holographic gratings, such as relying on experienced personnel, alignment blindness, long manufacturing periods, and insufficient alignment accuracy. Through theoretical modeling and simulations, the following conclusions can be stated: (1) the proposed moiré alignment algorithm for holographic gratings obtains real-time recording parameters of the exposure system, which helps to ensure the accuracy of alignment; (2) the multidegree of freedom physical model of the exposure system supplements the aberration expression, and gives the orthogonal basis of holographic grating aberration expressions for a rectangular aperture. These provide a theoretical basis for analyzing the holographic grating aberrations; (3) our moiré alignment algorithm provides better aberration-corrected holographic gratings, as it enhances the ability for aberration correction.

Funding. National Key Scientific Instrument and Equipment Development Project (2011YQ120023); Scientific and Technological Developing Scheme of Jilin Province (20150203021GX).

Acknowledgment. We would like to thank the National Engineering Research Center for Diffraction Gratings Manufacturing and Application for the use of their equipment.

REFERENCES

1. U. Bergmann, J. Corlett, S. Dierker, R. Falcone, J. Galayda, M. Gibson, J. Hastings, B. Hettel, J. Hill, Z. Hussain, C.-C. Kao, J. Kirz, G. Long, B. McCurdy, T. Raubenheimer, F. Sannibale, J. Seeman, Z.-X. Shen, G. Shenoy, B. Schoenlein, Q. Shen, B. Stephenson, J. Stöhr, and A. Zholents, *Science and Technology of Future Light Sources* (Atoms, 2008).
2. D. L. Voronov, T. Warwick, and H. A. Padmore, "Multilayer-coated blazed grating with variable line spacing and a variable blaze angle," Opt. Lett. **39**, 6134–6137 (2014).
3. C.-F. Xue, Y.-Q. Wu, Y. Zou, L. Xue, Y. Wang, Z.-J. Xu, and R.-Z. Tai, "A new extra-focus monochromator designed for high-performance VUV beamlines," J. Synchrotron Radiat. **22**, 328–335 (2015).
4. E. G. Loewen, G. Erwin, and E. Popov, *Diffraction Gratings and Applications* (Lasers Optics & Photonics, 1997).
5. T. Namioka, M. Seya, and H. Noda, "Design and performance of holographic concave gratings," Jpn. J. Appl. Phys. **15**, 1181–1197 (1976).
6. T. Namioka, "Theory of the concave grating II application of the theory to the off-plane eagle mounting in a vacuum spectrograph," J. Opt. Soc. Am. **49**, 460–465 (1959).
7. T. Namioka, "Theory of the concave grating. III. Seya-Namioka monochromator," J. Opt. Soc. Am. **49**, 951–959 (1959).
8. P. Kong, Y.-G. Tang, Bayanheshig, W.-H. Li, X. Tan, and J.-J. Cui, "Compensation effects between parameter errors of flat-field holographic concave gratings," Acta Opt. Sin. **31**, 0705001 (2011).
9. Y.-X. Jiang, Bayanheshig, S. Yang, X.-L. Zhao, N. Wu, and W.-H. Li, "Study on the effects and compensation effect of recording parameters error on imaging performance of holographic grating in on-line spectral diagnose," Spectrosc. Spectral Anal. **36**, 857–863 (2016).
10. I. M. Egdall, "Manufacture of a three-mirror wide-field optical system," Opt. Eng. **24**, 242285 (1985).
11. C. Palmer, "Theory of second-generation holographic diffraction gratings," J. Opt. Soc. Am. A **6**, 1175–1188 (1989).
12. Q. Zhou, X.-H. Li, K. Ni, R. Tian, and J.-C. Pang, "Holographic fabrication of large-constant concave gratings for wide-range flat-field spectrometers with the addition of a concave lens," Opt. Express **24**, 732–738 (2016).
13. C. G. Chen, P. T. Konkola, R. K. Heilmann, G. S. Pati, and M. L. Schattenburg, "Image metrology and system controls for scanning beam interference lithography," J. Vac. Sci. Technol. B **19**, 2335–2341 (2001).
14. M. L. Schattenburg and H. I. Smith, "The critical role of metrology in nanotechnology," Proc. SPIE **4608**, 116–126 (2002).
15. X. B. Zhu, S.-J. Fu, W.-Q. Ye, S.-P. He, J. Chen, X.-D. Xu, and Y.-L. Hong, "Explanation of the round interference fringes in the measurement of varied-line-space gratings," Opt. Precis. Eng. **10**, 634–638 (2002).
16. D. Malacara, *Optical Shop Testing*, 3rd ed. (Wiley, 2006), pp. 369–403.
17. G. A. Korn and T. M. Korn, *Mathematical Handbook for Scientists and Engineers* (McGraw-Hill, 1961).
18. S. Irie, T. Watanabe, H. Kinoshita, A. Miyafuji, K. Sugisaki, T. Oshino, and K. Murakami, "Development for the alignment procedure of three-aspherical mirror optics," Proc. SPIE **3997**, 807–813 (2000).
19. P. Hariharan, B. F. Oreb, and T. Eiju, "Digital phase-shifting interferometry: a simple error-compensating phase calculation algorithm," Appl. Opt. **26**, 2504–2506 (1987).
20. C. Joenathan, "Phase-measuring interferometry: new methods and error analysis," Appl. Opt. **33**, 4147–4155 (1994).
21. M. P. Rimmer, "A computer aided optical alignment method," Proc. SPIE **1271**, 363–368 (1990).
22. J. Zeng, Bayanheshig, W.-H. Li, and J.-P. Zhang, "Merit function to design holographic gratings for moderate-resolution monochromators," Appl. Opt. **50**, 6179–6183 (2011).